North Pacific Thermocline Variations on ENSO Timescales

ARTHUR J. MILLER, WARREN B. WHITE, AND DANIEL R. CAYAN

Climate Research Division, Scripps Institution of Oceanography, La Jolla, California

(Manuscript received 30 January 1996, in final form 4 March 1997)

ABSTRACT

The North Pacific thermocline (250 to 400 m) is studied using XBT observations acquired during the 1970s and 1980s. Interannual variations (3–5 yr timescales) in thermocline temperature, with $O(0.1°C)$ amplitude at 400 m, are found to exhibit westward propagation throughout the extratropical North Pacific up to 45°N. Southward of 30°N, the features propagate intact across the basin from the eastern boundary to the western boundary. Northward of 30°N, the features can be observed to propagate only as far as the date line. The observed midlatitude thermocline anomalies are often related to tropical ENSO events in that they occur most strongly after the development of tropical El Niño or La Niña conditions and propagate westward from near the eastern boundary in the midlatitudes. But it is found that the observed midlatitude thermocline anomalies have larger phase speeds than theoretically predicted free baroclinic Rossby waves. Also, the observed anomalies have larger wavelength and faster propagation speeds than baroclinic Rossby waves that radiate from coastal Kelvin-like waves near the eastern boundary in well-known high-resolution models.

Large-scale thermocline fluctuations that have spatial scale and phase speeds similar to the observations are also found in a coarse-resolution model of the Pacific Ocean forced by observed wind and heat flux anomalies over the 1970–88 period. In the midlatitudes, north of 30°N, large-scale Ekman pumping by interannual wind stress curl variations provides a significant driving mechanism for the modeled large-scale thermocline anomalies. The modeled ocean response is a combination of the static thermocline response to large-scale Ekman pumping plus a train of westward traveling Rossby waves, which accounts for part of the propagating temperature fluctuations. A tropical, remotely forced component is prominant near the eastern boundary, but this only contributes weakly in the model open ocean.

1. Introduction

Teleconnections from the tropical to the midlatitude North Pacific Ocean can occur in a variety of ways on interannual timescales associated with the El Niño–Southern Oscillation (ENSO) phenomenon (e.g., Philander 1990). Atmospheric teleconnections can carry information in wavelike disturbances that drive ocean responses in the extratropical North Pacific Ocean (e.g., Bjerknes 1966; Horel and Wallace 1981; Emery and Hamilton 1985; Alexander 1992). Among the oceanic teleconnections, the propagation of information northward from the Tropics along the eastern boundary via boundary-trapped Kelvin-like waves has been observed (e.g., Enfield and Allen 1980; Chelton and Davis 1982; Huyer and Smith 1985; Reinecker and Mooers 1986; Kessler 1990; White 1994). These observed boundary waves travel much slower than the Kelvin waves produced in shallow-water and primitive equation models (e.g., Pares-Sierra and O'Brien 1989; Johnson and O'Brien 1990; Shriver et al. 1991; Clarke and van Gorder 1994; Jacobs et al. 1994, Jacobs et al. 1996, manuscript submitted to *J. Geophys. Res.*, hereafter JHM; Meyers et al. 1996; Ramp et al. 1997). The relative importance of oceanic versus atmospheric mechanisms for transmitting information to the midlatitude ocean on ENSO timescales is not clear (e.g., Emery and Hamilton 1985; Johnson and O'Brien 1990; Norton and McClain 1994; Ramp et al. 1997) and the details of the physical processes involved have yet to be sorted out.

One signature of the midlatitude interior oceanic response on these timescales is a baroclinic wave field that can be generated remotely by radiation from poleward propagating boundary-trapped Kelvin-like waves or directly by atmospheric disturbances with ENSO timescales (e.g., White and Saur 1983; White 1985). Pares-Sierra and O'Brien (1989) compared the response of a shallow-water numerical model to local wind forcing and to oceanic forcing specified along the coastal strip at 18°N. They found ENSO-scale variations in sea level observed along the U.S. coast to be well correlated with equivalent sea level from the oceanically forced model, but they were not well correlated with those from the atmospherically forced model. The radiated baroclinic wave field propagating offshore in their model at 30°–40°N contained predominant wave-

Corresponding author address: Dr. Arthur J. Miller, Climate Research Division, Scripps Institution of Oceanography, University of California, La Jolla, CA 92093-0224.
E-mail: ajmiller@ucsd.edu

lengths of 800–1200 km. Further evidence included Shriver et al.'s (1991) identification of radiated baroclinic waves in a line of XBT observations off the western coast of North America at 45°N and Jacobs et al.'s (1994, JHM) demonstration that the radiated wave field associated with the 1982–83 El Niño propagated across the entire Pacific basin (10-yr transit time at 35°N) in both their numerical model and sea-level/SST observations.

A direct observation of basin-scale thermocline variations with ENSO timescales has not previously been obtained. Here we exploit a pan-Pacific XBT dataset to study 400-m temperature variations that have been processed to remove a monthly mean climatology. We find that westward propagating fluctuations do occur in the thermocline as far north as 45°N and that the signals are strongest after tropical El Niño or La Niña events. South of 30°N, they extend westward from the eastern to the western boundary, while at higher latitudes they extend only as far as the date line. At 30°–45°N, in contrast to the previously referenced high-resolution modeling studies, the directly observed midlatitude thermocline fluctuations occur with east–west wavelengths of approximately 3000 km and with larger phase speeds (2.4 cm s^{-1}) than anticipated by free baroclinic wave theory at these latitudes (cf. Chelton and Schlax 1996).

Furthermore, thermocline disturbances generated after the 1982–83 El Niño are observed to propagate across the midlatitude North Pacific as anticipated by Jacobs et al. (1994). These disturbances are arrested near the date line north of 30°N, however. Propagation of the thermocline variations at 30°N extends to the western boundary where they may influence the Kuroshio region as early as 1987–88, which implies a transbasin transit time in the observations of 4–5 years compared to the ten-year timescale found by Jacobs et al. (1994) in their study.

Similar interannual thermocline fluctuations occur in a coarse-resolution numerical ocean model that we use to diagnose some aspects of the thermocline variations. Statistical analysis of the model results suggest that interannual fluctuations of the basin-scale midlatitude wind system (associated with ENSO events via teleconnections to the Aleutian low) generate wind-stress curl fluctuations in the central North Pacific, which drive the midlatitude thermocline variations by Ekman pumping (cf. Bjerknes 1966; White et al. 1980; Horel and Wallace 1981; Emery and Hamilton 1985).

We commence our presentation with a discussion of the XBT data (§2) and the model simulation (§3), followed by an extended EOF analysis (§4) of the thermocline, velocity, and wind-stress curl fields (§5), and a summary of results (§6).

2. Ocean temperature dataset

The temperature data consists of all available XBT, CTD, MBT, and standard hydrographic observations over the period 1955–1992 assembled and quality controlled by the Scripps Joint Environmental Data Analysis Center. Processing of the raw hydrographic data to obtain anomalous temperatures at several standard depths from the surface to 400 m is described by White (1995). Since we wish to directly compare the data with a 1970–88 simulation, we only use data from the 1970–88 time period, which is also the best-sampled time interval. A monthly mean climatology was computed for the period 1970–88, and monthly temperature anomalies were defined with respect to that climatology. Seasonal (winter being Dec–Jan–Feb) anomalies were then computed using those monthly mean temperature anomalies at a series of standard levels to 400-m depth on a 5° longitude by 2° latitude grid. We wish to concentrate only on sub-mixed-layer thermocline variations in this study so that mixed layer processes do not directly influence the response. The observed mixed layer in the open ocean, away from the western boundary, generally does not exceed 250 m, so we considered only data from 250 m, 300 m, and 400 m. However, we found that all of the large-scale signals uncovered by our analysis are coherent between 250 and 400 m, with the variance decreasing with depth (resembling an equivalent barotropic response). Therefore, our discussion and analysis here will rely solely on the data at 400 m, which is less likely to be directly influenced by surface mixed layer processes than shallower levels.

3. 1970–88 ocean model simulation

The primitive equation ocean model was developed by Oberhuber (1993) and applied by Miller et al. (1994a,b) to study monthly mean through decadal-scale variations over the Pacific basin (60°N to 76°S). The model is constructed from eight isopycnal layers (constant potential density but variable thickness, temperature, and salinity) fully coupled to a bulk surface mixed layer model. As shown in Fig. 1, the resolution is relatively coarse (4° in open ocean, though with finer resolution near the equator and eastern/western boundaries), so only large-scale patterns can be studied with confidence. In particular, baroclinic coastal Kelvin-like waves, which are quasi-trapped to the horizontal model boundaries at the scale of the oceanic internal Rossby radius, occur in this model at a grid scale much larger than the observed Rossby radius. The surface forcing consists of a monthly mean seasonal cycle climatology of wind stress, total surface heat flux, and turbulent kinetic energy input to the mixed layer, to which are respectively added the specified monthly anomalies from 1970–88 derived from COADS observations. In the 20°S to 20°N latitude band, heat fluxes are parameterized as a Newtonian cooling to the model mean SST monthly mean climatology. There is no ocean feedback to the anomalous forcing so that the model is not constrained to reproduce the observed temperature variations. A thorough discussion of the model framework

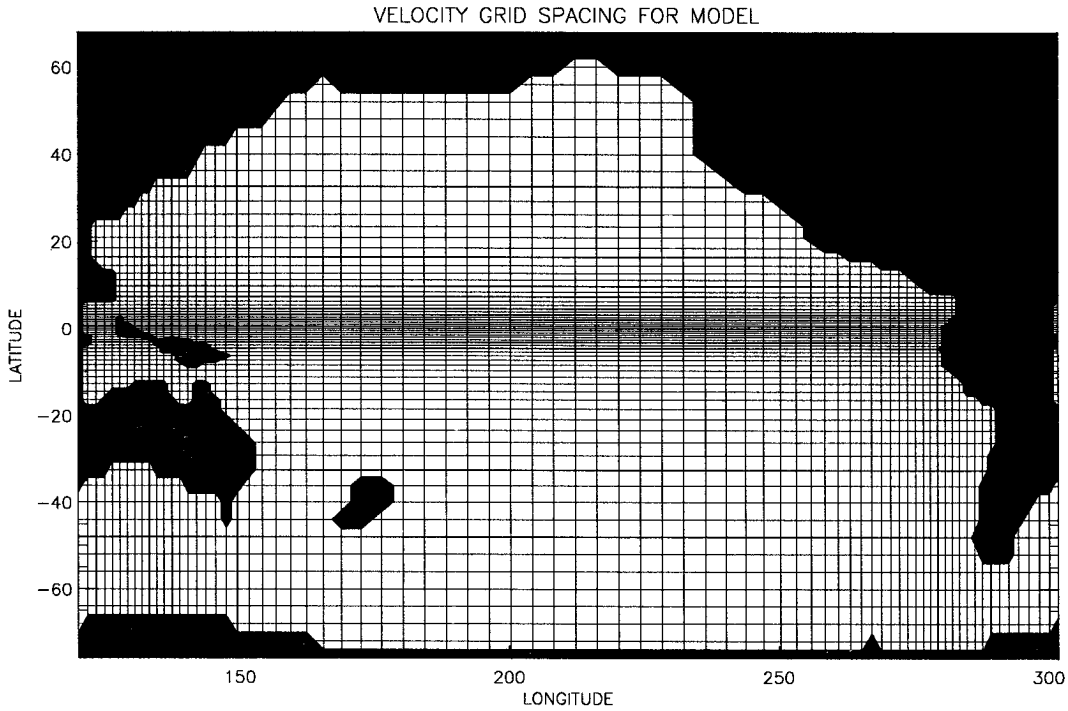

FIG. 1. Grid spacing for velocity points for the numerical simulation forced by observed winds and heat fluxes from 1970 to 1988. See Miller et al. (1994) for complete model details.

and forcing strategy is provided by Miller et al. (1994a,b) and Cayan et al. (1995).

Surface mixed layer variables were saved as true monthly mean quantities, but subsurface isopycnal layer fields were stored only once per month (on day 15). Even though monthly mean forcing fields were used, the model generates weak variability on shorter timescales for a variety of reasons so that the monthly sampling interval will result in some aliasing of these weak shorter timescale motions. We compared the monthly mean surface velocity fields with those day-15 monthly sampling fields and found that differences are typically less than 10% of the true monthly mean fields. Thus, by forming seasonal averages, we will have an even lower error for these estimates of the true model monthly mean fields at depth. Model climatologies for all the variables of interest (e.g., temperature and horizontal velocity at various depths, isopycnal depth variations, input wind-stress curl) were computed for the 1970–88 interval, and seasonal anomalies discussed below are relative to this monthly mean seasonal cycle state. Note that the model mixed layer never exceeded 230-m depth in the central North Pacific, so we can concentrate on anomalies at 250 m and greater when isolating ocean dynamics from mixed layer physics. As found in the observations the model response resembles an equivalent barotropic flow in the sense that 300-m anomalies are coherent with 400 m, but weaken with depth.

4. Extended EOF analysis

To isolate any propagating features of the thermocline anomalies, we used an extended empirical orthogonal function (EEOF) analysis. This technique has frequently been used in oceanographic and atmospheric problems to identify dominant pattern of space–time relationships (e.g., Weare and Nasstrom 1982; Robertson et al. 1995), specifically cyclical behavior in the field. It is essentially the same as multichannel singular spectrum analysis (Vautard and Ghil 1989). The covariance matrix is constructed with the original time series supplemented with time-lagged versions of the original time series. As the number of lags increases, the time series must be shortened, so there is a tradeoff between maximizing the degrees of freedom yet allowing the lags to span the interval of the oscillating feature. An excellent discussion of EEOFs is given by von Storch and Frankignoul (1996) in the context of many other techniques of statistical modal decomposition.

For several analyses herein, seasonal anomalies were constructed for all observed and modeled fields on a subgrid that approximately spanned 20° to 60°N and 160°E to the eastern boundary. (Any grid point without observations for one month was flagged and left out of the analysis.) This domain was chosen to (i) isolate the midlatitudes from the energetic variations with ENSO timescales that occur in the tropical strip, (ii) exclude the energetic region near the western boundary that is

coarsely sampled in observations and crudely modeled, and (iii) exclude the less well sampled lower latitude observations south of 20°N. The time interval of 1970–88 (more precisely December 1969 through November 1988) was selected for this analysis because (i) observations before 1970 are much more poorly sampled and (ii) the model simulation corresponds to that time interval so that the model can be directly compared to observations. The seasonal anomalies were extended by including seasonally lagged fields out to 3 years (13 total lags) from which the eigensolutions of the covariance matrix were computed. Thus, the time series of the EEOF coefficients runs from 1970 to 1985.

We also computed the combined extended EOFs of several pairs of variables to identify common patterns of propagation between the two fields. Other statistical techniques, such as canonical correlation analysis and singular value decomposition, could also be used, but Wallace et al. (1992) showed that robust signals will still be evident regardless of the selected statistical technique. If the fields were not the same unit, each field was normalized by a single number, the rms value of the field computed over the entire domain. Extended EOFs were computed for (i) XBT observations of 400-m temperature alone, (ii) observed and modeled 400-m temperature together, (iii) model 400-m temperature and model 400-m velocity together, and (iv) the important terms in the vertically integrated vorticity equation.

Questions regarding statistical significance of results necessarily arise with any statistical technique. Assumptions concerning noise in the system (the observed XBT dataset, the observed atmospheric model forcing, etc.) must be made so as to develop reliability statistics. The following discussion pertains to only the highest four eigenvalues of the system, which describe a relatively high amount of the variance, so we used an ad hoc method to estimate degrees of freedom in placing error bars on the eigenvalues. Moreover, the statistical results are substantiated by physical interpretation, which is a key point of validation.

5. Results

In the cases to be discussed, two predominant timescales emerge from the extended EOF analyses. The first EEOF, explaining roughly 25% of the temperature anomaly variance, has a decadal timescale and is discussed in a separate publication (Miller et al. 1997, manuscript submitted to *J. Climate*, hereafter MCW). (In the case with XBT observations alone, the second EEOF explains 8% of the variance and has a decadal timescale associated with a weak propagating component of the first EEOF mode.) The second most important signal, explaining roughly 10% of the variance, is a pair of extended EOFs (each explaining 5% of the variance) that are temporally and spatially lagged by approximately one-quarter cycle with respect to each other, indicating a propagating signal. The predominant timescale for these two modes is 3 to 4 years, with peak excitation associated with the well-known major warm and cold tropical (ENSO scale) events of the time interval. This pair of modes is the primary subject of the following discussion, categorized according to the EEOF input fields.

a. Observed 400-m temperature

When considering the XBT observations alone, we find the third and fourth EEOF modes together explain 10% of the total variance of the 400-m temperature seasonal anomaly field. Figure 2 shows the two modes for 4 of the 13 seasonal input lags, plotted at yearly intervals, along with the EEOF coefficient (principal component) time series at the bottom. The typical mid-latitude amplitude is 0.1°C (viz., the product of the spatial and temporal amplitudes). The two modes are phase lagged by approximately one year, as can be seen in Fig. 2, indicating a propagating feature. The progression from zero lag (top) to a three-year lag (lower) finds anomalies migrating westward from near the eastern boundary to at least 170°W. The EEOF time series reveal that the dominant propagating temperature variations occur after the 1972–73 and 1982–83 El Niño events; that is, the strong negative amplitude in 1975 and 1985 for EEOF-3 corresponds to a strong warm anomaly near 140°W in the eastern North Pacific. Using an ad hoc estimate of the degrees of freedom based on a one-year integral timescale (e.g., North et al. 1982) yields error bars of ± 0.32 times the eigenvalues (68% confidence intervals), which are appropriate for frequencies somewhat shorter than ENSO timescale. Error bars are half that range for the spectrum of high-frequency noise. The third and fourth eigenvalues are thus well separated from the noise background of the eigenvalue spectrum, which is red and drops well below unity for modes numbered greater than 25 (Fig. 2, bottom).

The pattern of the EEOFs repeats after approximately four years and has an east–west wavelength at 35°–40°N of roughly 3000 km, indicative of a phase speed of approximately 2.4 cm s^{-1}. Between 20° and 30°N, the east–west wavelength is longer, indicating much faster propagation speeds (exceeding 5 cm s^{-1}). The latitudinally dependent phase speed leads to a southwest to northeast arc in the temperature anomalies that resembles a Rossby wave front, as would be expected for the latitudinally dependent dispersion relation for baroclinic Rossby waves. However, these observed phase speeds are roughly twice as fast as theoretically anticipated phase speeds at these latitudes (e.g., Gill 1982, chapter 12), where the first-mode baroclinic wave speed is $c_p = -\beta a^2 = -\beta g H'/f^2$, where a is the Rossby radius, β is the meridional gradient of the Coriolis frequency f, g is the gravitational acceleration, and H' is the equivalent depth for the baroclinic mode. For example, using typical values of the Rossby radii computed from observations by Emery et al. (1984), we find $c_p = 1.4$ cm

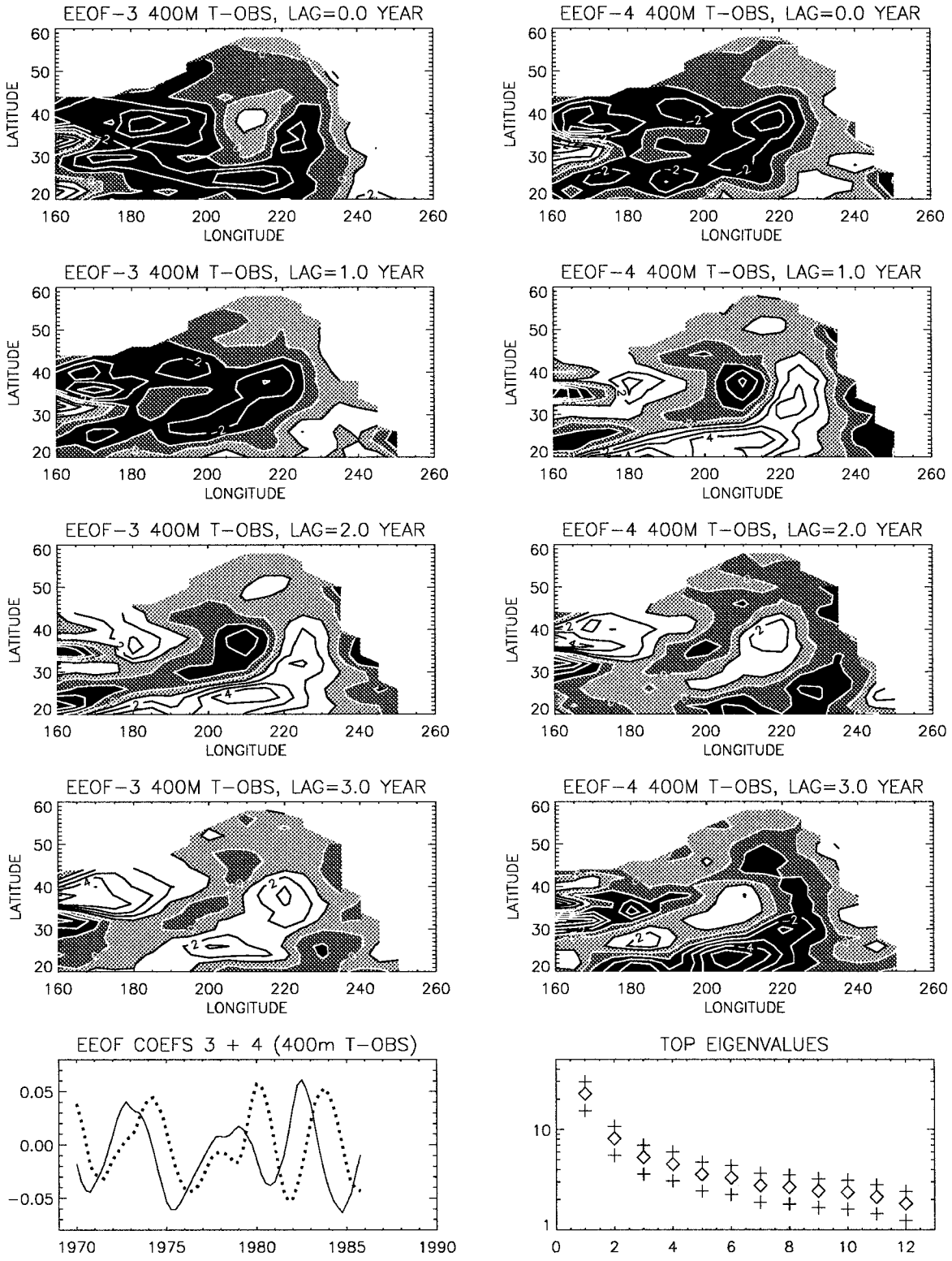

FIG. 2. Maps of EEOF-3 (left) and EEOF-4 (right) of seasonal anomalies of observed 400-m temperature in the reduced-domain North Pacific for (from top) 0-yr, 1-yr, 2-yr, and 3-yr lags (complete lags include 0 through 12 seasons). CI of 1°C, with black and dark gray shading negative, and light gray and white shading positive. (bottom) Principal component time series for (solid) EEOF-3 and (dotted) EEOF-4, and eigenvalue spectrum (diamonds) with 68% confidence intervals (plusses) based on ENSO timescale decorrelation time.

s^{-1} at 30°N ($a \approx 37$ km) and $c_p = 0.6$ cm s^{-1} at 40°N ($a \approx 27$ km). On the other hand, the present estimates are broadly consistent with the altimetric observations of sea-level anomaly propagation presented by Chelton and Schlax (1996).

The westward propagating features identified by the EEOFs are real and not an artifact of the analysis technique since they can also be seen clearly in maps of the raw temperature anomaly data. For example, the warm tropical event of 1982–83 can be followed across the North Pacific in low-passed animations[1] or in raw seasonal thermocline anomaly maps presented in Fig. 3 for the entire North Pacific Ocean. The left panels of Fig. 3 show fall season (Sep–Oct–Nov) total unfiltered anomaly maps for the 5-yr period 1984–88 after the 1982–83 ENSO for observed seasonal 400-m temperature anomaly fields (grayscale shading to enhance the contrast). The observations reveal the familiar pattern of baroclinic Rossby wave latitudinally dependent phase speed in the midlatitudes, with lower latitude anomalies propagating faster than those of the higher latitudes. As seen in the EEOFs (Fig. 2, n.b., the smaller analysis domain compared to Fig. 3), warm anomalies between 30°–45°N tend to propagate rapidly out to 160°W–180° where they are either arrested or swamped by ambient thermocline activity (associated with fluctuations of the Kuroshio Extension or driven by local wind-stress curl variations). Between 15° and 30°N, warm anomalies rapidly cross the basin until near the end of 1986 when they are replaced by propagation of cold anomalies. After that the warm anomalies near the western boundary (between 25° and 30°N) increase in amplitude and become stationary from 130°E to the date line. By fall 1988 warm anomalies associated with the 1986–87 ENSO have reached the lower latitude (south of 20°N) western boundary region. After this time the effects of the incoming 1986–87 warm anomalies overwhelm the remaining 1982–83 warm anomalies south of 30°N.

Thus, the thermocline anomalies associated with the 1982–83 El Niño cross the basin near 10°N in 1 year and at 30°N in about 4–5 years. At latitudes higher than 30°N, the observed thermocline anomalies generated in the eastern basin fail to cross the date line (but the local eddy field in the Kuroshio Extension may be obscuring further westward propagation). Near the western boundary, thermocline anomalies migrating northward from lower latitudes may also influence the Kuroshio. These results are similar to Jacobs et al.'s (1994, JHM) findings from a numerical model and surface observations (sea level, SST) of an intact wave front crossing the Pacific basin after 1982–83, but the transit time of the present observed subsurface features is much faster.

[1] These animations can presently be viewed at http://jedac.ucsd.edu, the Web site of the Joint Environmental Data Analysis Center at Scripps.

b. Observed and modeled 400-m temperature

The modeled 400-m temperature in Fig. 3 (right panels) shows that the westward propagating features in midlatitudes were reasonably well simulated. To gain additional insight into the dynamics involved in the observed westward propagating signal, we have executed an EEOF analysis of the model 400-m temperature data alone and also the observed and model 400-m temperature variations together. The results for the model 400-m temperature alone are so similar to the results of the combined model and observed EEOF analysis that only the latter needs to be shown here. The joint analysis identifies the spatial patterns of the temperature variations of the observations and model, which have similar time variations. Since the rms model temperature at 400 m is weaker than the observed, we have scaled each point by the monthly mean rms computed over the entire input domain (0.25°C for the observed and 0.13°C for the model).

The ENSO timescale pair of modes occur as the second and third EEOFs of the combined analysis, describing 7.9% and 7.0% of the normalized joint variance, respectively. Figure 4 presents a synopsis of the second EEOF showing its behavioral sequence through the three period of the 13 seasonal lags; this mode corresponds to EEOF-3 of Fig. 2. The combined model–observed 400-m temperature EEOF fluctuations share many features with the EEOF of observations alone (Fig. 2). The westward phase propagation in the eastern North Pacific is evident in both model and observed fields. The model anomalies have somewhat larger zonal and meridional length scales and also appear to have a slight northwestward propagation direction. The model also exhibits a smaller-scale northwestwardly propagating signal that originates near the date line and 25°–30°N and is reminiscent of a breaking baroclinic wave, which grows upon the strong north–south temperature and velocity gradient anomalies that occur there; no analog is evident in the data, so this feature will not be studied further here.

The combined mode has its strongest amplitude during the 1980s in association with the 1982–83 ENSO and its precursors. Compared with the time series of the observations in Fig. 2, the amplitude of the time series after the 1972–73 ENSO is much weaker in Fig. 4, indicating that the model is not capturing as large a propagating signal in the midlatitudes associated with that event. The correlation coefficients between the principal components of EEOF-2 of the combined model–observed analysis and EEOF-3 of the observational analysis is 0.66, and is 0.76 for EEOF-3 of the combined and EEOF-4 of the observed. These results suggest that the coarse-resolution model has captured the essential features of the observations and can be used to diagnose the dynamics of the prominant large-scale features.

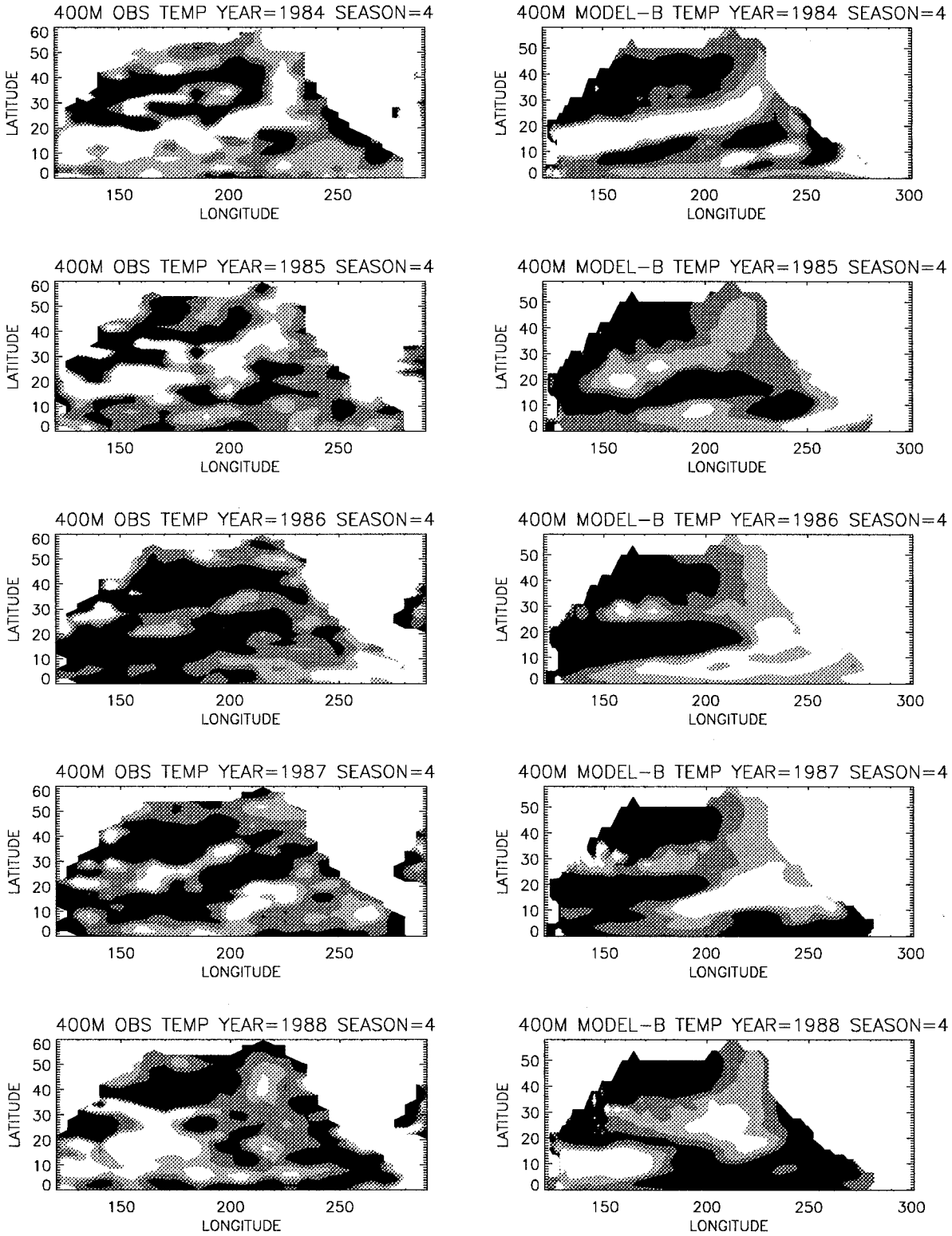

FIG. 3. Maps of (left) observed and (right) modeled anomalous 400-m temperature for fall seasons (Sep–Oct–Nov) for (from top) 1984 through 1988 in the entire North Pacific. The curved pattern of latitudinally dependent Rossby wave propagation is evident after the 1982–83 and the 1986–87 ENSOs. White regions greater than 0.1°C, black regions lower than −1°C, zero line separates light gray and dark gray regions. The contouring intervals are chosen to emphasize the similar structure between observed and modeled anomalies, but the observed temperature anomalies are approximately twice as large as those observed north of 30°N.

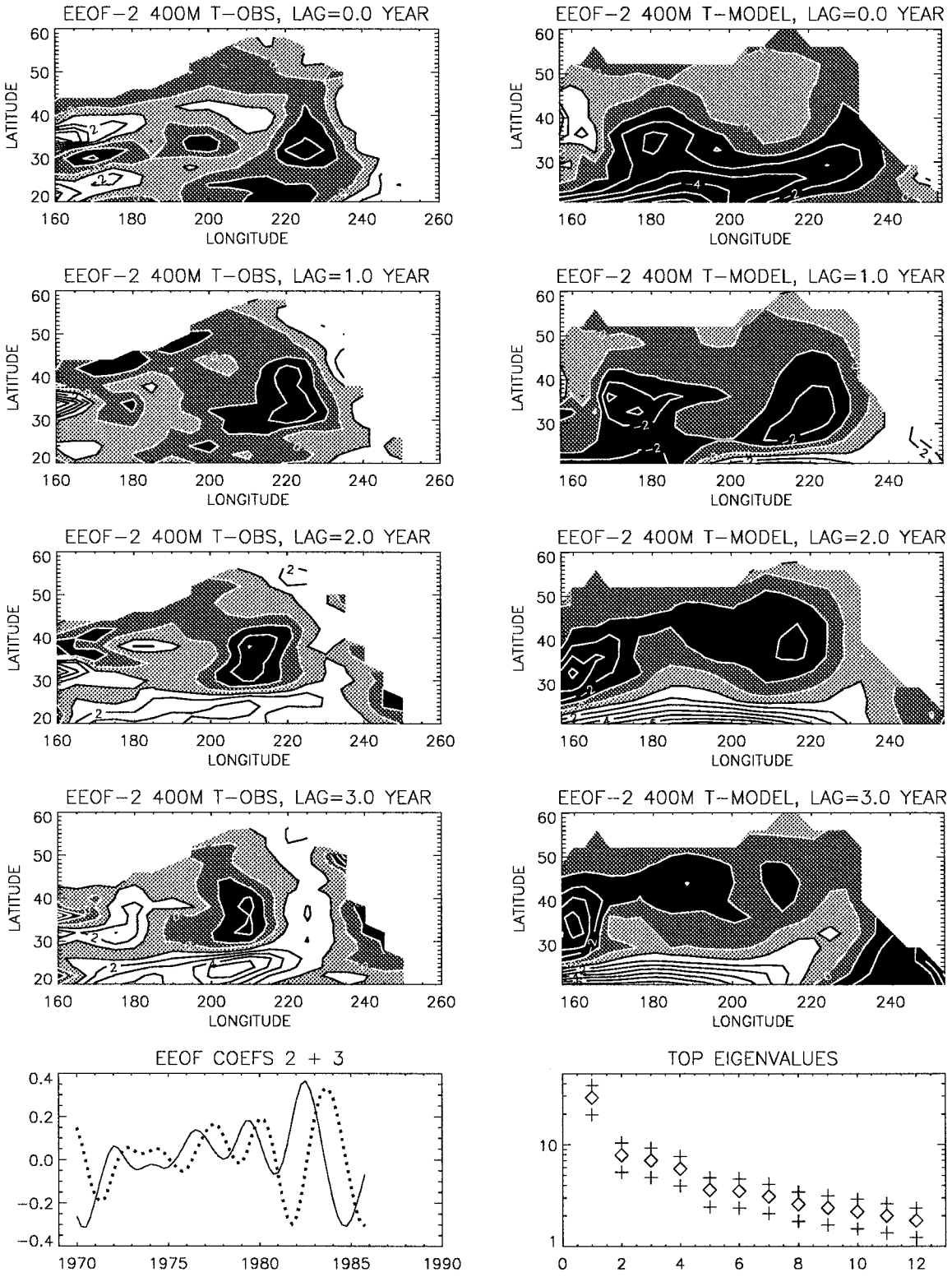

FIG. 4. Maps of combined EEOF-2 of seasonal anomalies of observed 400-m temperature (left, normalized by 0.25°C) and model 400-m temperature (right, normalized by 0.13°C) in the reduced-domain North Pacific for (from top) 0-yr, 1-yr, 2-yr, and 3-yr lags (complete lags include 0 through 12 seasons). CI of 1°C, with black and dark gray shading negative, and light gray and white shading positive. (bottom) Principal component time series for (solid) EEOF-2 and (dotted) EEOF-3, and eigenvalue spectrum (diamonds) with 68% confidence intervals (plusses) based on ENSO timescale decorrelation time.

c. Model 400-m temperature and velocity

To investigate the dynamics associated with the ENSO timescale thermocline anomalies we next evaluate the combined EEOFs of modeled 400-m temperature and velocity. The input fields are normalized by their rms values over the entire input domain, $T_{\rm rms} = 0.13°$ and $u = 0.35$ cm s^{-1}. Again, the second and third EEOFs represent the westward propagating signal previously identified from the temperature fields alone, now representing 11.3% and 10.8% of the normalized joint variance. The maps in Fig. 5 correspond to the same phase lags as Fig. 4 and indicate that the thermal anomalies are associated with large-scale velocity anomalies, which flow around the thermal anomalies in the sense of geostrophic flow. The velocity maps reveal large-scale coherent current anomalies that extend several thousand kilometers along the west coast of North America. Their magnitude along the eastern boundary exceeds 0.2 cm s^{-1} in the model, suggesting that observed anomalies would reach nearly 0.5 cm s^{-1} if we account for the weaker temperature signal found in the model vis-a-vis observations. As the temperature anomalies and the associated velocity anomalies migrate westward away from the boundary, the anomalous currents become more meridional and extend into/from the southern parts of the Alaska gyre. The temperature and velocity anomalies diminish after crossing 160°W more rapidly than expected from the observations that penetrate farther westward to near the date line. The principal components reveal time variations in the spatial patterns commensurate with those found for the previous two cases, which include observations. Thus, on interannual timescales associated with ENSO, the model indicates that the thermal anomalies are a large space-scale, dynamical feature in the midlatitude thermocline.

d. Midlatitude versus tropical forcing

The primary cause of these midlatitude thermocline deviations is likely to be either midlatitude atmospheric forcing or remote forcing from tropical atmosphere–ocean influences, via remote propagation of oceanic waves. In the midlatitudes, atmospheric forcing can be either local or remote in that waves could be forced locally near the eastern boundary and propagate westward from there. Concerning tropical forcing, the coarse resolution of the model precludes an accurate rendering of the oceanic process of coastal Kelvin-like waves arriving from the low latitudes. However, since coarse-grid analogs to properly resolved Kelvin-like waves do exist in the model (e.g., Hsieh et al. 1983; O'Brien and Parham 1992), we must distinguish which parts of the model response are forced in the midlatitudes and which parts propagate into the midlatitudes from the Tropics.

To sort this out, we have rerun the simulation described in section 3 and discussed in sections 5b,c for two additional cases. The first case (case E, for equatorial) includes no anomalous atmospheric forcing north of 20°N or south of 20°S. The second case (case M, for midlatitude) includes no anomalous atmospheric forcing south of 20°N. [A somewhat similar strategy was successfully employed by Pares-Sierra and O'Brien (1989) in their study of coastal sea level variability.] Both these cases started from the same initial conditions as the basinwide forcing case (case B), that is, 1 December 1969, which is the end state of an anomalously forced spinup period 1965–69. Because of this, it should be kept in mind that anomalous variability exists in the midlatitude initial conditions due to local and remote forcing effects of the 1965–69 period (although the previous analysis indicates that the largest influences occurred after the 1982–83 ENSO).

We recomputed 1970–88 monthly mean climatologies for temperature and currents in these two new cases. Figure 6 presents temperature anomaly maps for these two cases for comparison with Fig. 3 (right). In case M, the majority of the midlatitude temperature variability north of 20°N is recaptured with respect to case B. For case E, in contrast, the variability north of 20°N is weak compared to the cases B and M, although there is some penetration of signal to 30°N in the eastern basin. Case E shows the lower latitude (south of 20°N) westward propagation seen also in case B. This result suggests that midlatitude atmospheric forcing has considerable influence upon the ENSO-scale thermocline variations in the midlatitude regions north of 20°N. But it must be emphasized that the model's coarse resolution does not accurately represent the process of coastal Kelvin-like wave propagation from the Tropics and its consequent radiation into baroclinic Rossby waves.

We next examine the model velocity and temperature fields in these two new cases. Following section 5c, we computed combined EEOFs of model velocity and temperature at 400 m. The input fields are again normalized by their rms values over the entire input domain: Case M, $T_{\rm rms} = 0.11°$ and $u = 0.33$ cm s^{-1}, and case E, $T_{\rm rms} = 0.12°$ and $u = 0.21$ cm s^{-1}. (Since the velocity and temperature fields are normalized, one should only compare the structures but not the magnitude of signals among plots in Figs. 5 and 7.) As in previous cases, the first EEOF corresponds to a decadal timescale, while the second and third EEOFs form a propagating pair with interannual timescales. For brevity, Fig. 7 shows only one phase lag for each EEOF for these two cases, along with their principal components. (Note that the EEOFs have different space–time phasing among the three cases.) The phase lag selected in the plot corresponds approximately to the time when the oscillation has its largest temperature magnitude in the midlatitude open ocean north of 25°N. For case M (Fig. 7, left), the large-scale thermal fluctuations north of 30°N seen in case B (Fig. 5, lag 1.0 yr) are evident. For case E (Fig. 7, middle), a weaker version of the baroclinic Rossby wave front seen in case B (Fig. 5, lag 2.0 yr) is found in the temperature field. The large meridional-scale ve-

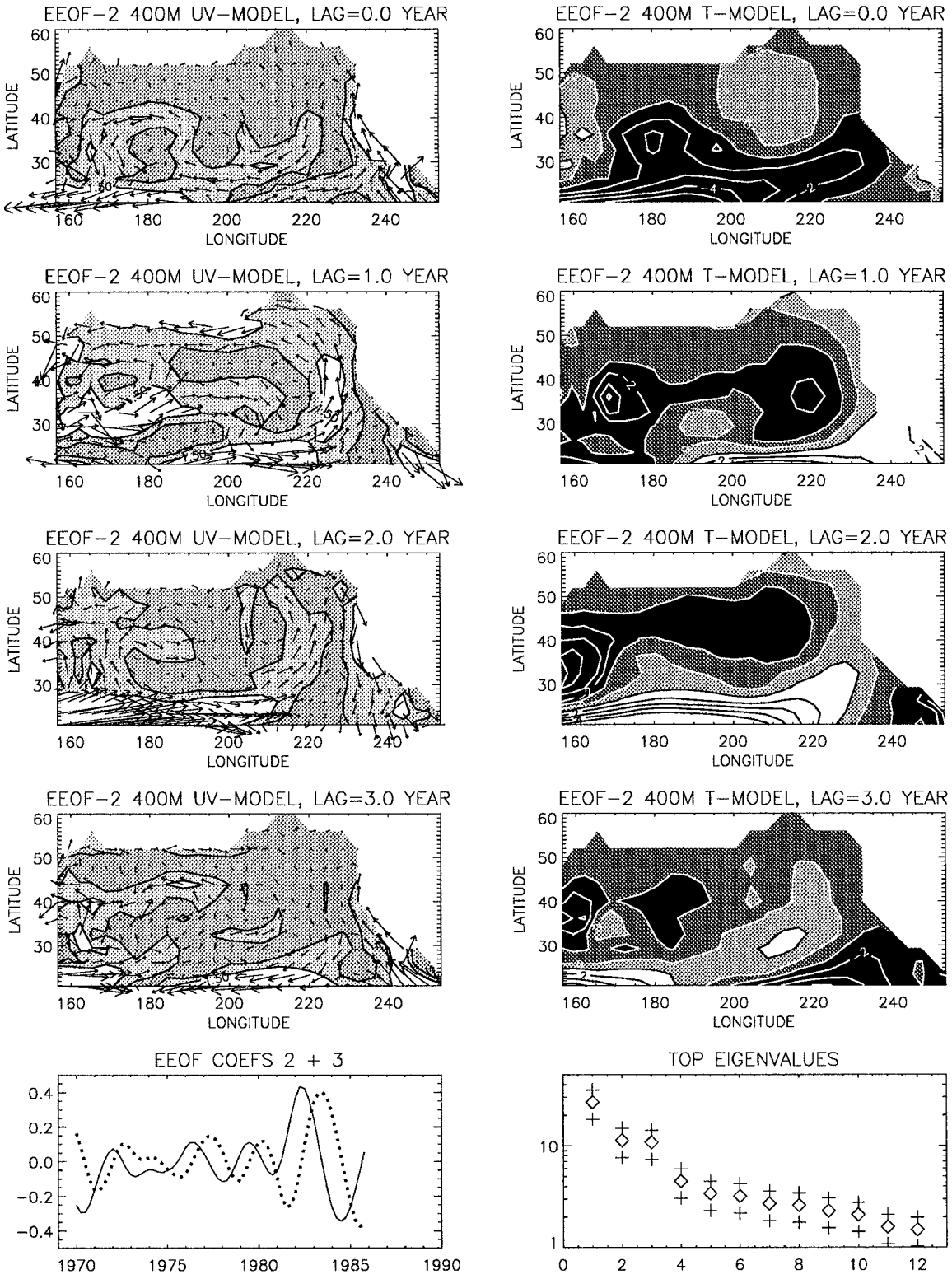

FIG. 5. Maps of combined EEOF-2 of seasonal anomalies of modeled 400-m velocity (left, normalized by 0.35cm s^{-1}) and modeled 400-m temperature (right, normalized by 0.13°C) in the reduced-domain North Pacific for (from top) 0-yr, 1-yr, 2-yr, and 3-yr lags (complete lags include 0 through 12 seasons). CI of 1°C for temperature and 0.75 cm s^{-1} for velocity, with darker values smaller and lighter values larger. (bottom) Principal component time series for (solid) EEOF-2 and (dotted) EEOF-3, and eigenvalue spectrum (diamonds) with 68% confidence intervals (plusses) based on ENSO timescale decorrelation time.

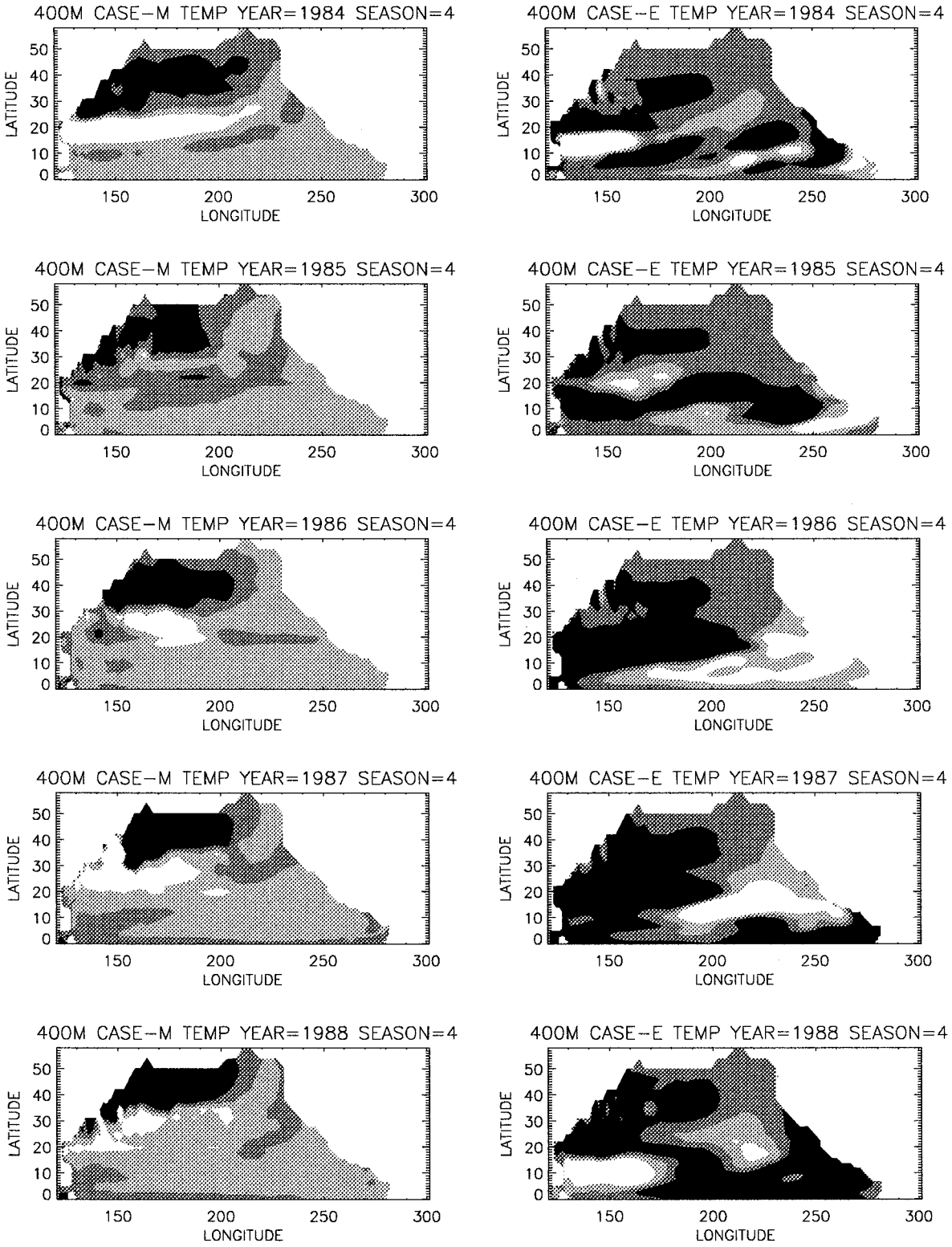

FIG. 6. Same as Fig. 3 (right) but for (left) case M, midlatitude forcing, and (right) case E, equatorial forcing.

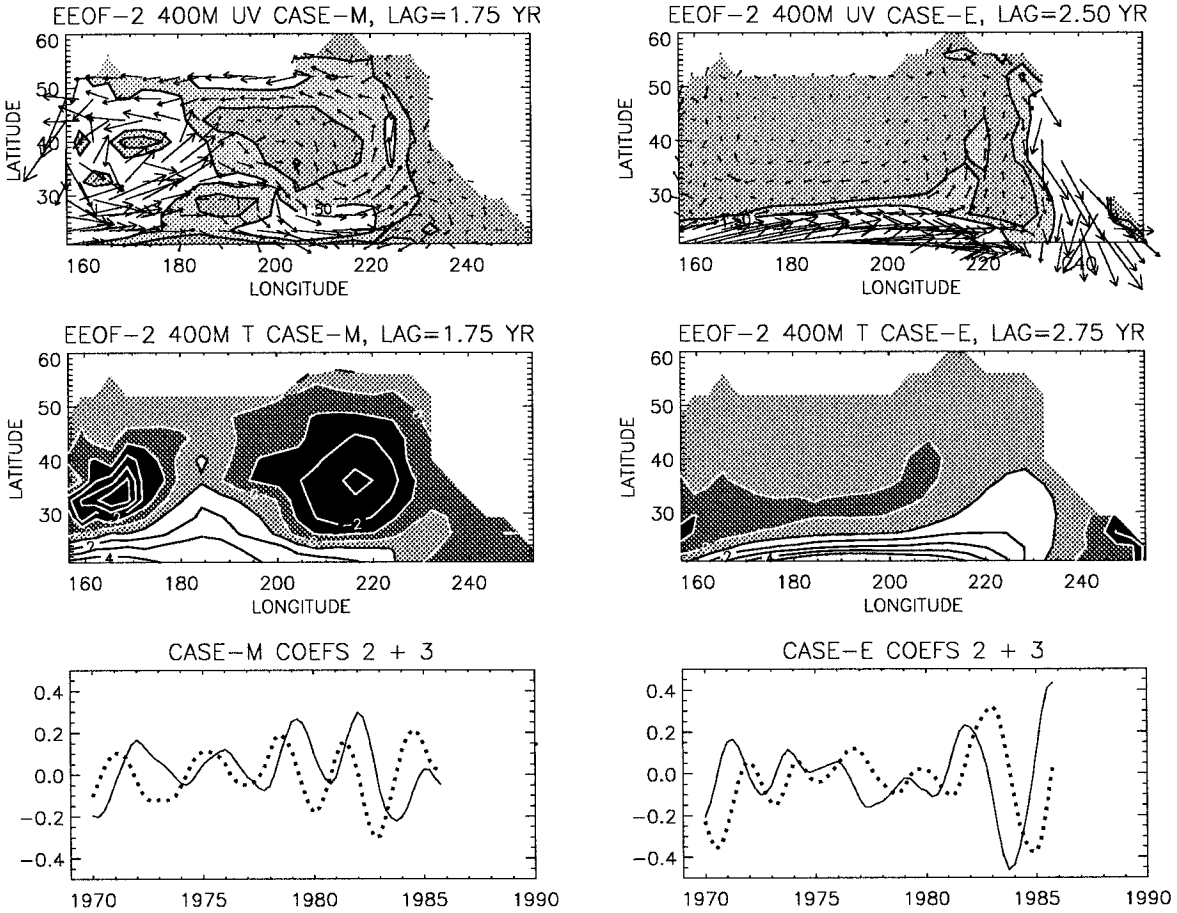

FIG. 7. (Left) Case M map of one phase (lag 1.75 yr) of combined EEOF-2 of seasonal anomalies of modeled 400-m velocity (top, normalized by 0.33 cm s^{-1}) and modeled 400-m temperature (middle, normalized by 0.11°C) in the entire North Pacific. Compare with Fig. 5, lag 1.0 yr. (Right) Same as top but for case E, lag 2.75 yr (normalized by 0.21 cm s^{-1} and 0.12°C). Compare with Fig. 5. (Bottom) Principal component time series for (solid) EEOF-2 and (dotted) EEOF-3 for (left) case M and (right) case E.

locity anomalies along the west coast of North America are clearly driven by equatorial processes in case E. These model Kelvin-like waves radiate weakly into the eastern ocean interior. In case M, large meridional-scale velocity anomalies are also created, but with largest amplitude in the ocean interior region and little coastal signature. The EEOF coefficients for case E exhibit stronger variations during the 1982–83 and 1986–87 ENSO events as would be expected for a run forced only by tropical forcing by which ENSO events are usually defined. The EEOF coefficients for case M reveal ENSO timescale events but also include non-ENSO interannual variations during the late 1970s.

The combination of the midlatitude and equatorial forcing effects is thus evident in case B. The alongshore coastal velocity signal is due to equatorial forcing, while the large-scale temperature anomalies north of 30°N are predominantly due to midlatitude forcing. Associated with those open-ocean temperature anomalies generated in the midlatitudes are large-scale velocity anomalies (in the sense of geostrophic flow). South of 30°N, it is uncertain how strongly radiation from the model's coastal Kelvin-like waves controls the westward propagating response since anomalous low-latitude winds south of 20°N are included in case E. Furthermore, it should be noted that the artificial nature of the anomalous atmospheric wind stress forcing, that is, a step function across 20°N in cases M and E, may lead to spurious oceanic wave excitation since the consequent wind stress curl along 20°N is unrealistic and possibly large amplitude. Nonetheless, these two experiments each produce distinct components of the midlatitude model response. It is interesting that the east–west wavelength and the north–south spatial structure of the velocity fields in cases E and M are similar in the midlatitudes and the anomalously forced responses likely reinforce each other in case B.

e. Vertically integrated vorticity equation

We next seek to identify the character of the midlatitude forcing that contributes to the midlatitude tem-

perature anomalies driven in the model and seen in the data. Since we are examining thermocline fluctuations well below the mixed layer, we anticipate that ocean dynamics will play the major role. Therefore, we sought a relation between input wind-stress curl forcing and the velocity anomalies by studying the vertically integrated (from 0 to 1500 m) vorticity equation,

$$\zeta_t + \beta v + f\delta = \frac{\text{curl}\tau}{\rho H} + D, \tag{1}$$

where ζ is the vertically integrated vorticity, δ is the vertically integrated horizontal divergence, v is the vertically integrated meridional velocity, τ is the wind stress, D is damping, f is the latitudinally dependent Coriolis parameter, and β is its latitudinally dependent meridional derivative.

The relative vorticity term in (1) is much smaller than the other terms on these timescales, and damping is sufficiently small to be disregarded. We therefore seek large-scale relations among the three dominant terms in (1), the divergence term (proportional to deflection of the lower interface by the continuity equation, i.e., vortex stretching), the beta term, and the Ekman pumping term,

$$\beta v + f\delta \approx \frac{\text{curl}\tau}{\rho H}. \tag{2}$$

Because complete model fields were archived only once per month, the terms in Eq. (1) must be reconstructed and an exact balance of terms each month is not achievable. The results of the following statistical analysis (the terms of which also are not exactly balanced), however, suggest that the large-scale patterns of variability among the terms can nonetheless be identified.

To suppress higher frequency wind-stress curl variations and possible aliasing due to the monthly archiving, we averaged over two seasons in a three-term combined EEOF (seven 2-season lags out to three years) of Eq. (2). The first two combined EEOFs of case B explain 20% of the 6-month anomaly combined variance, 10.9% and 9.4%, respectively. This pair of modes corresponds to the interannual, ENSO-scale variations we have previously identified, as can be seen by the time variability and the spatial patterns. Figure 8 shows combined EEOF-1 for the beta term, the divergence term, the Ekman pumping term, and the sum of the three terms according to (2). Combined EEOF-1 (Fig. 8) of this case leads combined EEOF-2 (Fig. 5) of the case with currents and temperature by about 6 months. As can be seen, the statistical analysis has extracted the three dominant terms, which when summed produce a small residual except west of the date line where smaller-scale wave excitation is evident and near the land boundaries where the effective wind stress curl is influenced by the boundaries.

While an interdecadal-scale thermocline change has a component nearly in quasi-Sverdrup balance (beta term nearly balancing curl τ term) in the eastern basin (MCW), on interannual timescales a different balance operates. The scale of the curl τ anomalies is large, indicating that they are associated with interannual variations of the midlatitude wind system. The wind stress curl patterns are also well matched in space to the location of the Aleutian low. The time variability of these EEOFs (Fig. 8, bottom) has maxima associated with most of the major ENSO events of the time interval and is more highly correlated with the principal components of case M than case E, as would be expected for an analysis that includes midlatitude wind forcing. The figure indicates that these wind stress curl fluctuations are well matched to the spatial patterns of divergence in the central North Pacific (Ekman pumping driving thermocline displacement). The ocean adjusts to these basin-scale Ekman pumping variations by sending out westward propagating baroclinic Rossby waves (e.g., Anderson and Killworth 1977), which have small amplitude near the eastern boundary in case M (section 5d). North–south transport fluctuations in the open ocean, which were previously associated with ENSO-scale 400-m temperature variations (cf. Figs. 4, 5, 7, and 8), are thus excited by the large-scale pattern of wind stress curl in Fig. 8. The total open ocean response is the sum of the particular solution (directly forced temperature fluctuations from the large-scale Ekman pumping) plus the transients (Rossby waves emanating from near the east boundary) needed to satisfy the boundary conditions. Since the atmospheric forcing is time-dependent and stochastic, the transients are continually excited.

Concurrent with the process of basin-scale adjustment adjustment to midlatitude forcing, coastal Kelvin-like waves arriving from the equatorial region excite longshore meridional velocity fluctuations along the eastern boundary (cf. Figs. 5, 7, and 8). These waves (as seen in (section 5d) radiate weakly into the ocean interior and have a very weak temperature and velocity signal offshore, which tends to be in phase with the midlatitude atmosphere's forced response. These waves are evident by the balance of the beta term with the divergence term in Fig. 8. This equatorially driven model balance is mainly confined to the eastern basin and also south of 30°N, and it corresponds to the remotely propagating signal identified in previous sections. In the central North Pacific, the wavelike thermocline fluctuations are overwhelmed by the static thermocline fluctuations driven locally by Ekman pumping. An analogous EEOF analysis for the vorticity equation of case M (midlatitude forcing) reveals that the magnitude of the βv term is reduced by up to one-half in the open ocean, and the alongshore transport anomalies are nearly absent (as previously seen in §5d).

These results strongly suggests that the wind stress curl drives a significant fraction of the the large-scale interannual (ENSO scale) thermocline deviations, and that forcing by remote waves from the Tropics, which

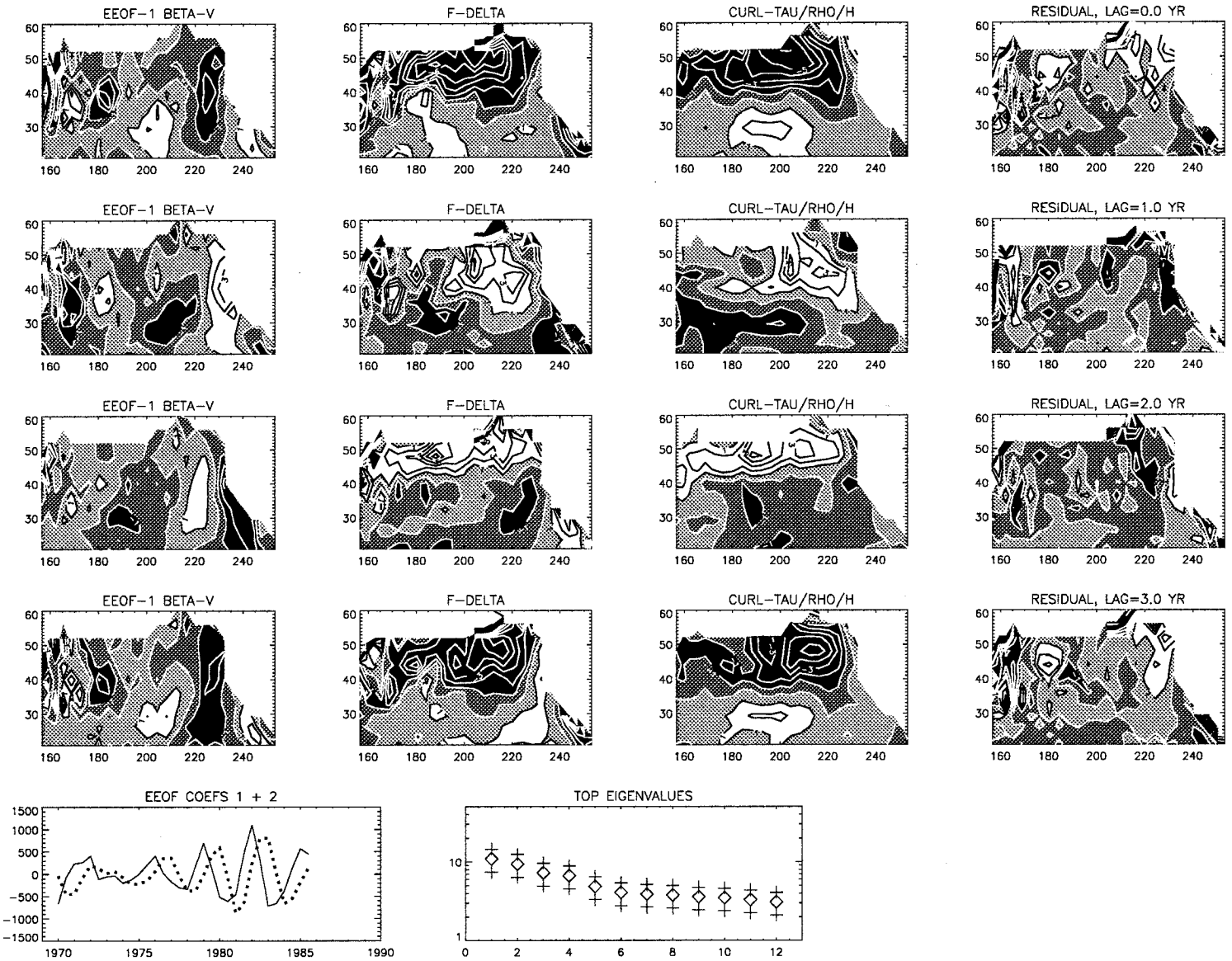

FIG. 8. Maps of combined EEOF-1 of 6-month anomalies of the three dominant terms of the vertically integrated (0–1500 m) vorticity equation (2). (Left) divergence term, (center) beta term, and (right) curl τ term in the reduced-domain North Pacific for (top to bottom) 0-yr, 1-yr, 2-yr, and 3-yr lags. CI of 1 s^{-2}, with black and dark gray shading negative, and light gray and white shading positive. (bottom) Time series of (solid) EEOF-1 and (dotted) EEOF-2, and eigenvalue spectrum (diamonds) with 68% confidence intervals (plusses) based on ENSO timescale decorrelation time.

is correlated to the midlatitude atmospheric variations, plays a secondary role north of 25°N. Because the Ekman-pumping-forced thermocline anomalies do not have sufficient time to adjust to the time-dependent interannual forcing (to form a Sverdrup balance), baroclinic waves are excited as transients that propagate phase westward from the eastern basin as the ocean attempts to equilibrate the directly forced interior region. At the same time, weak radiation from model coastal Kelvin-like waves arriving from the Tropics drives a smaller amplitude interior ocean response, which appears to be in phase with the midlatitude wind-forced response. Of course, a coarse-resolution[2] model such as employed here is not expected to properly resolve the radiation process, which may partly explain the reason why the model westward propagating temperature anomalies north of 25°N are somewhat smaller amplitude and larger scale than the observed. But the wind-forced portion of the midlatitude response is likely to be reasonably well represented. Since the wind-stress curl anomalies have such large meridional (25°–55°N) and zonal (180°–130°W) scale, and since the thermocline anomalies and their corresponding velocity fields have commensurately large scales (larger than found in published high-resolution modeling studies), we conclude that the midlatitude ENSO-scale model thermocline variability is significantly influenced by basin-scale midlatitude wind stress curl fluctuations.

6. Discussion and summary

A two-decade history of observed 400-m temperature (thermocline) anomalies reveals a propagating signal in the middle latitudes of the North Pacific at ENSO timescales. The propagating anomalies can be seen in raw basinwide temperature anomaly maps and are captured as a pair of EEOF modes, which together explain 10% of the total 400-m temperature variance. Although the amplitude at 400 m is only $O(1°C)$, the spatial scale is large. These thermocline fluctuations can be traced over halfway across the North Pacific to 175°W in the latitude band 30°–45°N. At latitudes south of 30°N, they reach the western boundary. Neither SST anomalies nor upper-ocean (0–400 m) heat content anomalies have been shown to propagate this far west northward of 30°N (cf. Herrara-Cervantes and Pares-Sierra 1994; White and Cayan 1997, manuscript submitted to *J. Climate*). But this should not be too surprising since the anomalous SST is dominated by local atmospheric forcing, predominantly surface heat fluxes (e.g., Cayan 1992). The thermocline fluctuations considered here occur beneath the mixed layer and are effectively insulated from direct interactions (thermal coupling and turbulent mixing) with the atmosphere. Thus, in spite of the sparse sampling in space and time this dataset contains a coherent signal with interannual timescales associated with El Niño.

These observed ENSO-timescale thermocline anomalies differ from the radiated baroclinic waves found in highly resolved ocean models influenced by coastally trapped Kelvin-like waves of equatorial origin (e.g., Pares-Sierra and O'Brien 1989; Shriver et al. 1991; Pares-Sierra 1991; Jacobs et al. 1994; Meyers et al. 1996). First, these observed thermocline anomalies have longer east–west wavelengths at 30°–45°N than the radiated analogs, roughly 3000 km compared to 800–1200 km. The phase speed of the anomalies is therefore also larger (2.4 cm s^{-1}) than expected theoretically. Recently, Chelton and Schlax (1996) have found that sea level fluctuations derived from altimeter data also tend to propagate westward at speeds higher than expected for the sea level signature of internal Rossby waves; at 30°–45°N our observed thermocline phase speeds fall in the range of those associated with their sea level data. Last, while we have found them to decay (or become obscured) near the date line for latitudes between 30° and 45°N, it has been shown that highly resolved model thermocline anomalies can propagate across the Pacific basin (Jacobs et al. 1994, JHM). At slightly lower latitudes the anomalies appear to reach the western boundary in roughly half the time (4–5 yr) expected from theoretical arguments. However, the present results do not preclude the occurrance of the shorter-wavelength waves or transbasin propagation north of 30°N since they may be inadequately sampled by this observational dataset.

A numerical simulation, using a coarse-resolution ocean general circulation model forced by 1970–88 observed monthly winds and fluxes, captured many aspects of the observed open ocean thermocline fluctuations. Consequently, we used it to identify dynamic aspects of the response unobtained from XBT observations alone. Because both model and observations have similar responses, we have more confidence in these results than if we had analyzed either field in isolation. The observations cannot provide a dynamically consistent image of reality due to uncertainties in both the output signal (250–400-m temperature) and the input forcing. The model can provide a dynamically consistent representation of output response to the specified input forcing (even though that forcing function is only an estimate for the true input to the real ocean). Thus, our philosophy is that common features of the model and observed output response are likely to be real signals so their dynamics can be elucidated by the model.

The model enabled us to show that the ENSO-scale thermocline anomalies are associated with large-scale velocity fluctuations (in the sense of geostrophic flow) that are coherent over large scales along western North America. Two additional simulations, one which in-

[2] Yukimoto et al. (1996) also report westward propagating ENSO-scale thermocline variations at 32°N that are apparently forced by Ekman pumping in a fully coupled ocean–atmosphere model with midlatitude oceanic resolution of approximately 2°.

cluded only anomalous atmospheric forcing north of 20°N and the second which included only anomalous forcing south of 20°N, revealed that crudely modeled coastal Kelvin-like waves arrive from the Tropics and dominate the model alongshore velocity field fluctuations. On the other hand, in the interior North Pacific the thermocline response was mainly forced by the midlatitude atmosphere. In this region, the large-scale thermocline response is commensurate with the scale of Aleutian low PNA-like variations associated with ENSO conditions. Using the vertically integrated vorticity equation, it was clear that the model thermocline and velocity anomalies were significantly driven in the interior ocean by large-scale wind-stress curl fluctuations associated with the stochastic ENSO-scale fluctuations of the Aleutian low (cf., Bjerknes 1966; Horel and Wallace 1981; Emery and Hamilton 1985).

These results support the contention that extratropical wind stress variations drive a significant fraction of midlatitude ENSO-scale open ocean activity (e.g., White et al. 1980; Simpson 1984; Huyer and Smith 1985; Reinecker and Mooers 1986; Johnson and O'Brien 1990; Norton and McLain 1994); a recent study by Ramp et al. (1997) showed that a high-resolution model of the 1991–93 ENSO forced by observed winds contained both atmospheric and oceanic teleconnections that contributed to the oceanic response off California. Our results complement those coastal and near-coastal studies in that interior ocean midlatitude ENSO-scale thermocline anomalies appear to be largely driven by Ekman pumping.

Acknowledgments. Funding was provided by NOAA under the Scripps Experimental Climate Prediction Centre (NA36GPO372, NA67GPO450) and the Lamont/Scripps Consortium for Climate Research (NA47GPO188), the National Space Development Agency of Japan, and (to AJM) by the G. Unger Vetlesen Foundation. AJM thanks M. Alexander, G. Auad, D. Battisti, T. Baumgartner, D. Chelton, C. Deser, G. Jacobs, P. Lermusiaux, J. McClean, S. Meyers, J. O'Brien, and A. Pares-Sierra for discussions and/or preprints of their work. The two reviewers provided exceptional comments and motivated the additional two model cases discussed in §5d.

REFERENCES

Alexander, M. A., 1992: Midlatitude atmosphere–ocean interaction during El Niño. Part 1: The North Pacific Ocean. *J. Climate,* **5,** 944–958.

Anderson, D. L. T., and P. D. Killworth, 1977: Spin-up of a stratified ocean, with topography. *Deep-Sea Res.,* **24,** 709–732.

Bjerknes, J., 1966: A possible response to the atmospheric Hadley circulation to equatorial anomalies of temperature. *Tellus,* **18,** 820–829.

Cayan, D. R., 1992: Latent and sensible heat flux anomalies over the northern oceans: Driving the sea surface temperature. *J. Phys. Oceanogr.,* **22,** 859–881.

——, A. J. Miller, T. P. Barnett, N. E. Graham, J. N. Ritchie, and J. M. Oberhuber, 1995: Seasonal-interannual fluctuations in surface temperature over the Pacific: Effects of monthly winds and heat fluxes. *Natural Climate Variability on Decadal-to-Century Time Scales,* National Academy of Sciences Press, 133–150.

Chelton, D. B., and R. E. Davis, 1982: Monthly mean sea-level variability along the west coast of North America. *J. Phys. Oceanogr.,* **12,** 757–784.

——, and M. G. Schlax, 1996: Global observations of oceanic Rossby waves. *Science,* **272,** 234–238.

Clarke, A. J., and S. van Gorder, 1994: On ENSO coastal currents and sea levels. *J. Phys. Oceanogr.,* **24,** 661–680.

Emery, W. J., and K. Hamilton, 1985: Atmospheric forcing of interannual variability in the northeast Pacific Ocean. *J. Geophys. Res.,* **90,** 857–868.

——, W. G. Lee, and L. Magaard, 1984: Geographic and seasonal distributions of Brunt–Väisälä frequency and Rossby radii in the North Pacific and North Atlantic. *J. Phys. Oceanogr.,* **14,** 294–317.

Enfield, D. B., and J. S. Allen, 1980: On the structure and dynamics of monthly mean sea level anomalies along the Pacific coast of North and South America. *J. Phys. Oceanogr.,* **10,** 557–578.

Gill, A. E., 1982: *Atmosphere-Ocean Dynamics.* Academic Press, 662 pp.

Herrara-Cervantes, H., and A. Pares-Sierra, 1994: Propagacion de variaciones de baja frecuencia en la temperatura superficial del Pacifico nor-oriental. *Geofis. Int.,* **33,** 469–486.

Horel, J. D., and J. M. Wallace, 1981: Planetary atmospheric phenomena associated with the Southern Oscillation. *Mon. Wea. Rev.,* **109,** 813–829.

Hsieh, W. W., M. K. Davey, and R. C. Wajsowicz, 1983: The free Kelvin wave in finite-difference numerical models. *J. Phys. Oceanogr.,* **13,** 1383–1397.

Huyer, A., and R. L. Smith, 1985: The signature of El Niño off Oregon. *J. Geophys. Res.,* **90,** 7133–7142.

Jacobs, G. A., H. E. Hurlburt, J. C. Kindle, E. J. Metzger, J. L. Mitchell, W. J. Teague, and A. J. Wallcraft, 1994: Decade-scale trans-Pacific propagation and warming effects of an El Niño anomaly. *Nature,* **370,** 360–363.

——, ——, and J. L. Mitchell, 1996: Decadal variations in ocean circulation. Part I: Rossby waves in the Pacific. *J. Geophys. Res.,* in press.

Johnson, M. A., and J. J. O'Brien, 1990: The Northeast Pacific Ocean response to the 1982–1983 El Niño. *J. Geophys. Res.,* **95,** 7155–7166.

Kessler, W. S., 1990: Observations of long Rossby waves in the northern tropical Pacific. *J. Geophys. Res.,* **95,** 5183–5219.

Meyers, S. D., M. A. Johnson, M. Liu, J. J. O'Brien, and J. L. Spiesberger, 1996: Interdecadal variability in a numerical model of the northeast Pacific Ocean. 1970–89. *J. Phys. Oceanogr.,* **26,** 2635–2652.

Miller, A. J., D. R. Cayan, T. P. Barnett, N. E. Graham, and J. M. Oberhuber, 1994a: Interdecadal variability of the Pacific Ocean: Model response to observed heat flux and wind stress anomalies. *Climate Dyn.,* **9,** 287–302.

——, ——, ——, ——, and ——, 1994b: The 1976–77 climate shift of the Pacific Ocean. *Oceanography,* **7,** 21–26.

North, G. R., T. L. Bell, R. F. Cahalan, and F. J. Moeng, 1982: Sampling errors in the estimation of empirical orthogonal functions. *Mon. Wea. Rev.,* **110,** 699–706.

Norton, J. G., and D. R. McLain, 1994: Diagnostic patterns of seasonal and interannual temperature variation off the west coast of the United States: Local and remote large-scale atmospheric forcing. *J. Geophys. Res.,* **99,** 16 019–16 030.

Oberhuber, J. M., 1993: Simulation of the Atlantic circulation with a coupled sea ice–mixed layer–isopycnal general circulation model. Part I: Model description. *J. Phys. Oceanogr.,* **23,** 808–829.

O'Brien, J. J., and F. Parham, 1992: Equatorial Kelvin waves do not vanish. *Mon. Wea. Rev.,* **120,** 1764–1767.

Pares-Sierra, A., 1991: Remote and local forcing of Rossby wave

variability in the midlatitude Pacific Ocean. *Geofis. Int.,* **30,** 121–134.

——, and J. J. O'Brien, 1989: The seasonal and interannual variability of the California Current System. *J. Geophys. Res.,* **94,** 3159–3180.

Philander, S. G. H., 1990: *El Niño, La Niña and the Southern Oscillation.* Academic Press, 293 pp.

Ramp, S. R., J. L. McClean, C. A. Collins, A. J. Semtner, and K. A. S. Hays, 1997: Observations and modeling of the 1991–1992 El Niño signal off central California. *J. Geophys. Res.,* **102,** 5553–5582.

Reinecker, M. M., and C. N. K. Mooers. 1986: The 1982–83 El Niño signal off northern California. *J. Geophys. Res.,* **91,** 6597–6608.

Robertson, A. W., C.-C. Ma, C. R. Mechoso, and M. Ghil, 1995: Simulation of the tropical Pacific climate with a coupled ocean–atmosphere general circulation model. Part I. The seasonal cycle. *J. Climate,* **8,** 1178–1198.

Simpson, J. J., 1984: A simple model of the 1982–83 Californian ''El Niño.'' *Geophys. Res. Lett.,* **11,** 243–246.

Shriver, J. F, M. A. Johnson, and J. J. O'Brien, 1991: Analysis of remotely forced oceanic Rossby waves off California. *J. Geophys. Res.,* **96,** 749–757.

Vautard, R., and M. Ghil, 1989: Singular spectrum analysis in nonlinear dynamics with application to paleoclimatic time series. *Physica D,* **35,** 395–424.

von Storch, H., and C. Frankignoul, 1996: Empirical modal decomposition in coastal oceanography. *The Sea, The Global Coastal Ocean,* in press.

Wallace, J. M., C. Smith, and C. S. Bretherton, 1992: Singular value decomposition of wintertime sea surface temperature and 500-mb height anomalies. *J. Climate,* **5,** 561–576.

Weare, B. C., and J. N. Nasstrom, 1982: Examples of extended empirical orthogonal function analyses. *Mon. Wea. Rev.,* **110,** 481–485.

White, W. B., 1985: The resonant response of interannual baroclinic Rossby waves to wind forcing in the eastern midlatitude North Pacific. *J. Phys. Oceanogr.,* **15,** 403–415.

——, 1994: Slow El Niño–Southern Oscillation boundary waves. *J. Geophys. Res.,* **99,** 22 737–22 751.

——, 1995: Design of a global observing system for gyre-scale upper ocean temperature variability. *Progress in Oceanography,* Vol. 36, Pergamon Press, 169–217.

——, and J. F. T. Saur, 1983: Sources of interannual baroclinic waves in the eastern subtropical North Pacific. *J. Phys. Oceanogr.,* **13,** 531–544.

——, R. Bernstein, G. McNally, S. Pazan, and R. Dickson, 1980: The thermocline response to transient atmospheric forcing in the interior midlatitude North Pacific 1976–1978. *J. Phys. Oceanogr.,* **10,** 372–384.

Yukimoto, S., M. Endoh, Y. Kitamure, A. Kitoh, T. Motoi, A. Noda, and T. Tokioka, 1996: Interannual and interdecadal variabilities in the Pacific in an MRI coupled GCM. *Climate Dyn.,* **12,** 667–683.